Tunable H2/Syngas Production by Chemical Looping Reforming of Methane over La0.6Sr0.4MxM'1 x(M,M' = Fe, Mn, Co)O3 Perovskites

ChemCatChem

Research Article
doi.org/10.1002/cctc.202500554

Chemistry Europe
European Chemical Societies Publishing

www.chemcatchem.org

Tunable H_2/Syngas Production by Chemical Looping Reforming of Methane over $La_{0.6}Sr_{0.4}M_xM'_{1-x}$(M,M′ = Fe, Mn, Co)$O_3$ Perovskites

Stefano Scognamiglio,[a, b] Anna Basco,[a] Melania Musone,[a] Alessandra Di Nardo,[a] Giulia Sorbino,[a] and Gianluca Landi*[a]

The applications of perovskites in chemical looping dry and steam reforming have shown promising results in efficient hydrogen production from hydrocarbons. Notably, $LaFeO_3$ has shown exceptional capabilities in reforming processes, with surface oxygen contributing to the complete oxidation of methane to CO_2 and H_2O, while bulk lattice oxygen promotes partial methane oxidation to H_2 and CO. In this study, the effect of B-site substitution in $La_{0.6}Sr_{0.4}B_xB'_{1-x}O_3$ (B, B′ = Fe, CO, Mn) was systematically investigated with the aim to develop a material with enhanced redox properties and selectivity to syngas. Among the synthesized materials, under cyclic operation at 900 °C, $La_{0.6}Sr_{0.4}Fe_{0.6}Mn_{0.4}O_3$ (LSFM) demonstrated improved redox activity, stability, and reproducibility. In addition, an innovative three-step redox cycle is proposed in this study: (i) methane reduction at 900 °C, producing H_2-rich syngas and coke deposition, (ii) steam oxidation at 550 °C, producing pure H_2 and reoxidation of the material, and (iii) steam oxidation at 900 °C, which gasifies the coke into syngas. Structural characterization indicated increasing perovskite stability with cycling by secondary phases disappearing while redox properties were unaffected. These results highlight the potential of Sr- and Mn-substituted perovskites as efficient and durable oxygen carriers for chemical looping reforming.

1. Introduction

During the last years, there has been a renewed interest in the production and utilization of hydrogen.[1–3] Hydrogen has been recognized as a potential energy carrier due to several desirable characteristics, including high energy density, zero greenhouse gas emissions when utilized, and the potential for various applications, thus enabling decarbonization of several strategic sectors, including transportation, power generation, and industrial processes.[3] Currently, hydrogen can be produced by several processes, including steam methane reforming (SMR), coal gasification, biomass gasification, and water electrolysis,[4] using both fossil and renewable sources as feedstocks.

In this framework, concentrated solar thermal (CST) technologies use solar radiation as a renewable heat source that, among the different applications, can be used to drive endothermic reactions, thus enabling thermochemical energy storage (TCES) in chemical compounds such as hydrogen.[5] Most of TCES processes consist of chemical looping cycles, by which a solid material undergoes two or more reaction steps cyclically.[6,7] The production of hydrogen (H_2), carbon monoxide (CO), or a mixture of them (synthesis gas) is pursued. Thermochemical splitting of water (H_2O) and carbon dioxide (CO_2) is an example and consists of a high-temperature reduction step of a metal oxide with the release of gaseous oxygen, followed by an oxidation step of the reduced oxide using H_2O and\or CO_2, producing H_2 and\or CO.[8–11] However, the reduction step typically requires temperatures of 1200 °C–1500 °C and extremely low O_2 partial pressures, typically obtained by vacuum pumping or inert-gas sweeping.[8–11] The introduction of a reducing agent, such as methane, allows more moderate thermodynamic conditions and the simultaneous production of syngas during the reduction step. The resulting overall reaction in this case is known as Chemical Looping Reforming (CLR) and is considered as a cutting-edge technology for hydrogen production.[3] Several CLR processes were developed using different feedstocks, such as natural gas, oil, and ethanol;[12] in these processes, oxygen carriers were based on transitional metal (Ni, Cu, Mn, and Fe) oxides.[12]

In case of methane used as feedstock, the reactions involved in the reduction step are as follows.

$$CH_4 + \frac{1}{\delta}MO_x \rightarrow CO + 2H_2 + \frac{1}{\delta}MO_{x-\delta} \quad (1)$$

$$CH_4 + \frac{4}{\delta}MO_x \rightarrow CO_2 + 2H_2O + \frac{4}{\delta}MO_{x-\delta} \quad (2)$$

[a] S. Scognamiglio, A. Basco, M. Musone, A. Di Nardo, G. Sorbino, G. Landi
Institute of Science and Technology for Sustainable Energy and Mobility, CNR, Piazzale Vincenzo Tecchio, Naples 80-80125, Italy
E-mail: gianluca.landi@cnr.it

[b] S. Scognamiglio
Department of Applied Science and Technology (DISAT), Polytechnic University of Turin, C.so Duca degli Abruzzi, Turin 24-10129, Italy

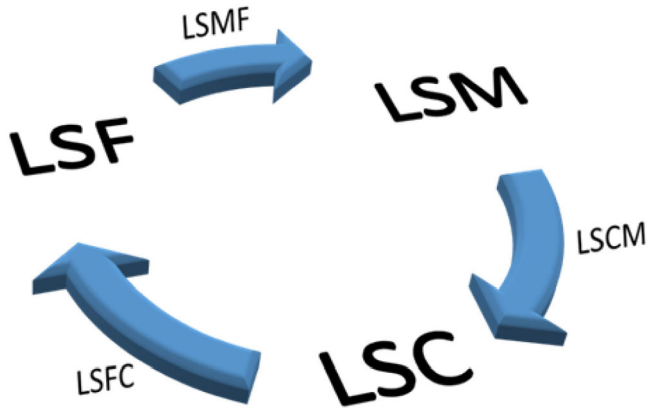

Figure 1. Rationale of the materials preparation.

$$CH_4 \rightarrow C + 2H_2 \quad (3)$$

where MO_x and $MO_{x-\delta}$ represent the oxidized and reduced metal oxide, respectively. Equations (1) and (2) represent the partial and total oxidation of the fuel, respectively, while Equation (3) represents fuel decomposition.

In CLR, a high fuel conversion and selectivity to syngas are desirable; to achieve high fuel conversion, a large oxygen storage capacity (OSC) is required, related to flexible oxygen migration rates, while a high syngas can be achieved by matching the oxygen migration rate within the oxygen carrier with the rate of surface catalytic reactions.[13]

The key factor for the development of CLR process is the selection of suitable metal oxides showing low reduction temperatures, high re-oxidation rates, high oxygen capacities (δ), tunable surface reaction rate, and good stability over cycles.[12] Metals like nickel and iron oxides, due to their high abundance, alongside cobalt and ceria, are particularly well-suited for these applications and have been extensively studied in this context. Numerous studies have explored the combination of these oxides, such as Ni and Fe supported on ceria or zirconia[14,15] while other works have focused on the development of novel metal oxide-based catalysts incorporating tungsten, like Ni-modified tungstate zirconia and $MnWO_4$, $NiWO_4$.[16,17] These materials demonstrate significant catalytic activity, particularly at milder temperatures (700 °C–850 °C), making them suitable for a variety of processes.

Thanks to their structural and electronic properties, perovskites are gaining more attention for CLR at higher temperatures (above 850 °C), where their enhanced stability and redox capabilities offer distinct advantages. Perovskites (general formula ABO_3) are non-stoichiometric oxygen carriers proposed for CLR.[12,18–20] $LaFeO_3$-based oxygen carriers were the most investigated perovskites as CLR materials.[12,21] Several works reported the effect of partial substitution of A and/or B cations.[22–33] Cobalt is often used as a co-cation in B position,[22,23,27–32] leading to improved performance due to higher structural disorder/distortion.[28] Moreover, cobalt and iron can display a synergistic effect on the selectivity to syngas during the reduction step with methane due to their deep reduction and fast oxygen diffusion from the bulk to the surface.[29] Sr has been used to partially substitute La as A-site;[24–31] the lower valence of samarium with respect to lanthanum introduced charge compensation by B cations and/or oxygen vacancy and/or structural disorder, causing larger OSC and faster reduction/oxidation kinetics.

While Mn-based perovskite ($LaMnO_3$) was largely used as combustion oxygen carriers,[12] its use as CLR material is limited.[34–38] As for Fe-based perovskites, Sr is the most common substitute for La as A-cation; its effect on the redox properties is like that reported for $LaFeO_3$-based materials.[38] Redox properties were also improved by acting on B site; both reducible (Ni, Cu, Fe, and Cu)[35,36,38] and non-reducible (Al)[37] elements were employed. Results reported a consensus on the positive effect of B-substitution due to the addition of active sites and the formation of oxygen vacancies. Moreover, Mn-based perovskites generally show a lower activity toward methane decomposition.[36]

In previous work, we demonstrated that partial substitution of the B cation in $La_{0.6}Sr_{0.4}MnO_3$ (LSM) is an effective strategy to tailor the redox properties toward H_2O splitting.[39] In this study, we extended and rationalized this effect, underlying the role of different B cations (Mn, Fe, Co) in the CLR with methane as the reducing agent and steam as the oxidizing agent to produce H_2-rich mixtures. It is worth noting that a comprehensive study of the combined effect of these three metals (according to the rationale reported in Figure 1) has never been reported. Moreover, on the best material, high-temperature cyclic operation has been carried out to assess both performance and stability under applicative operating conditions. Finally, according to the intriguing features of our materials, a novel three-step cycle has been proposed and assessed.

2. Materials and Methods

2.1. Materials

Perovskites with La/Sr = 1.5 and variable B cation molar ratios were prepared according to the procedure described elsewhere.[39] Briefly, aqueous solutions, prepared by mixing stoichiometric amounts of nitrates (manganese (II) nitrate tetrahydrate, iron (III) nitrate nonahydrate, cobalt (II) nitrate hexahydrate, strontium nitrate, lanthanum nitrate hydrate (Sigma–Aldrich)), were heated in a MW oven (CEM SAM-155; 10 min) up to the formation of a homogeneous gel. Calcination at 1100 °C for 6 h (heating rate: 10 °C/min) in a high-temperature furnace provided the perovskite. The nominal composition of the prepared samples can be described by the general formula $La_{0.6}Sr_{0.4}B_{1-x}B'_xO_3$ ($0 \leq x \leq 1$; *B*, *B'*: Fe, Mn, Co). In Table 1, the general formulas and labels for the prepared materials are reported.

The Goldschmidt tolerance factor is a key parameter used to assess the structural stability of perovskite materials. It is defined as.

$$t = \frac{r_A + r_O}{\sqrt{2}\,(r_B + r_O)} \quad (4)$$

Table 1. Prepared catalysts, their nominal formulas, surface areas, and labels.

Material	Label	SSA, $m^2/g^{a)}$	SSA, $m^2/g^{b)}$
$La_{0.6}Sr_{0.4}MnO_3$	LSM	3.5	3.1
$La_{0.6}Sr_{0.4}Mn_{0.6}Fe_{0.4}O_3$	LSMF	2.7	2.3
$La_{0.6}Sr_{0.4}Mn_{0.4}Fe_{0.6}O_3$	LSFM	3.8	5.0
$La_{0.6}Sr_{0.4}FeO_3$	LSF	2.2	3.5
$La_{0.6}Sr_{0.4}Co_{0.4}Fe_{0.6}O_3$	LSFC	2.2	3.7
$La_{0.6}Sr_{0.4}CoO_3$	LSC	1.8	0.9
$La_{0.6}Sr_{0.4}Co_{0.4}Mn_{0.6}O_3$	LSMC	2.7	3.2

[a] Fresh samples.
[b] Used samples.

where r_A is the ionic radius of the A-site cation, r_B is the ionic radius of the B-site cation, and r_O is the ionic radius of the oxygen anion. An ideal perovskite structure, which is cubic, corresponds to a tolerance factor close to 1. In practice, perovskites typically exhibit a tolerance factor ranging from 0.8 to 1.1, with deviations indicating varying degrees of structural distortion depending on the relative sizes of the cations and the anions.

The analyzed perovskites exhibit a Goldschmidt tolerance factor ranging from 0.85 to 0.87, which theoretically defines their structure as rhombohedral.[40]

2.2. Materials Characterization

The actual composition was determined by means of ICP-MS analysis using an Agilent 7500CE instrument. Results showed differences with the nominal content within the experimental error (±5.0%).

BET surface areas (SSA) of supports and catalysts were measured by N_2 adsorption at 77 K with a Quantachrome Autosorb-1C instrument after degassing the samples at 150 °C for 1.5 h. Results on fresh and used samples are reported in Table 1. SSA are lower than 5 m^2/g due to the high-temperature treatment.[23]

X-ray diffraction spectra were collected with an XRD diffractometer PANalytical X'Pert Pro. The measurements were carried out with a step size of 0.02° and a counting time of 80 s per step.

O_2-TPO was carried out in the experimental setup described elsewhere[39] on used samples to evaluate the deposition of coke. Experiments were performed in 2 vol.% O_2/N_2 by heating up to 1000 °C (heating rate: 10 °C/min; isothermal step at 1000 °C: 20 min).

2.3. CLR Tests

The powdered catalysts (0.5 g) were tested in the experimental setup described elsewhere[39] and without any pretreatment. Catalytic tests were conducted at a constant contact time, defined as the ratio of catalyst weight to flow rate, set at 0.18 $g{\cdot}s{\cdot}cm^{-3}$. Two distinct sets of measurements were carried out.

A preliminary screening of the redox properties of the materials was carried out by two TPR/TPO cycles. Reduction was performed in 5 vol.% CH_4/N_2 by heating up to 1000 °C (heating rate: 10 °C/min; isothermal step at 1000 °C: 20 min). The reduced sample was cooled down to 300 °C in N_2. Then, oxidation was performed in 5 vol.% H_2O/N_2 by heating up to 1000 °C (heating rate: 10 °C/min; isothermal step at 1000 °C: 20 min).

A selected sample was tested for isothermal CLR. Reduction and oxidation mixtures were identical to those used in the preliminary screening, with varying temperatures between 800 °C and 900 °C. Stability of the material was tested by repeating isothermal cyclic operation (reduction/oxidation) at 900 °C for 40 cycles. Finally, several non-isothermal three-step cycles (reduction at 900 °C; first oxidation at 550 °C; second oxidation at 900 °C) were carried out to check the performance of a novel cycle proposed in this work.

The molar amount of gaseous species *i* produced or consumed (n_i) was calculated from the volumetric composition (y_i) (Equation 5), assuming the total molar flow rate (F) constant due to the high dilution of the stream. Consequently, the performance evaluation was carried out through methane conversion x_{CH4} (Equation 6) and product selectivity s_i (Equation 7).

$$n_i = N \int y_i^{IN} - y_i^{OUT} dt \quad (5)$$

$$x_{CH_4} = \frac{n_{CH_4}^{IN} - n_{CH_4}^{OUT}}{n_{CH_4}^{IN}} \quad (6)$$

$$S_i = \frac{n_i^{OUT}}{\sum_i n_i^{OUT}} \quad (7)$$

3. Results and Discussion

3.1. TPR/TPO

Figure 2 shows the concentration profiles of the gaseous species recorded during the two TPR/TPO cycles on LSM. During the first cycle, reduction reaction started at about 600 °C with a peak in CH_4 consumption at 1000 °C along with a peak of production of H_2, CO, and CO_2. CO_x production is directly related to material reduction. Interestingly, CO selectivity is significantly higher than CO_2 selectivity (Table 2), suggesting the production of high-value syngas. The transition to a more gradual and stable methane consumption after the peak can be attributed to the formation of carbon deposits due to methane decomposition. However, a non-negligible CO production is detected; under these operating conditions, material reduction is limited by oxygen diffusion from the bulk to the surface.[29] During the subsequent oxidation step, H_2 production was first noticed at relatively low temperatures (<600 °C); the absence of contemporary CO_x production suggests that the so-produced hydrogen is the product of the oxidation of the perovskite. At higher temperatures (600–1000 °C), H_2, CO, and CO_2 were found to be produced simultaneously, suggesting the occurrence of coke gasification

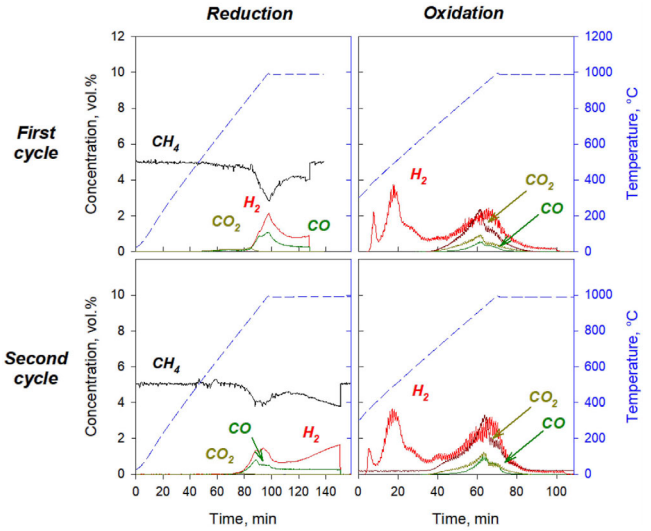

Figure 2. Concentration profiles during TPR/TPO cycles on LSM.

according to Equations (8) and (9).

$$C + H_2O \rightarrow CO + H_2 \quad (8)$$

$$C + 2H_2O \rightarrow CO_2 + 2H_2 \quad (9)$$

Interestingly, H_2 concentration calculated according to Equations (8) and (9) (dark red line in Figure 2) overlaps the measured profile in the high-temperature range, suggesting that only coke gasification occurs within these operating conditions. Thus, full perovskite oxidation occurs at low temperatures. On LSM, CO_2 production during TPO is slightly higher than CO production, in agreement with the good activity of Mn-based perovskites toward full oxidation.[41–43]

The second TPR/TPO cycle shows similar qualitative behavior of the first one, even if the reaction rates are slower and the concentrations of the gases produced and consumed are lower and higher, respectively.

Figure 3 shows the concentration profiles of the gaseous species recorded during the two TPR/TPO cycles on LSFM. LSFM exhibits similar behavior from a qualitative perspective to LSM. As for LSM, methane is converted to syngas during TPR due to material reduction, while an additional H_2 production is related to methane decomposition at high temperatures and a high reduction degree of the material. This finding agrees with the results of DFT calculations on $LaFeO_3$, suggesting that coke deposition by methane decomposition occurs on reduced iron.[44] During TPO, the low-temperature H_2 production can be assigned to LSFM re-oxidation, as reported above for LSM, while the high-temperature H_2 evolution, occurring simultaneously to CO_x production, is exclusively due to coke gasification (dark red line in Figure 3 represents H_2 concentration calculated according to Equations (8) and (9).

The quantitative behavior of LSFM during TPR/TPO is significantly different from that reported for LSM. Methane conversion and product evolution are significantly higher; CO_2 production is very low, resulting in a CO-rich syngas produced. Also, syngas produced by coke gasification during TPO is richer in CO than in CO_2, confirming the good activity of iron toward partial rather than full oxidation.[12] Additionally, the second cycle shows a qualitative and quantitative behavior similar to the first one, suggesting a better stability of LSFM than LSM.

Other materials show similar TPR/TPO cycles (not reported). Table 2 shows the performance of the different perovskites. It is worth noting that methane conversion during TPR is low due to the long inactivity of the materials between room temperature and about 600 °C; actually, the performance cannot be compared to literature results. Except for LSM showing the low-

Table 2. Performance of perovskites in TPR/TPO cycles.

		Reduction							Oxidation							
First cycle		x_{CH4}	s_{CO}	s_{CO2}	s_C	s_{H2}	H_2/CO_x	CO/CO_2	x_{H2O}	s_{CO} [a]	s_{CO2} > [a]	s_{CO} > [b]	s_{CO2} > [b]	s_O > [b]	H_2/CO_x	CO/CO_2
	LSC	15	8.9	9.6	81.5	71.9	7.8	0.9	28.8	91.3	8.7	64.4	24.6	11.1	1.2	10.5
	LSF	19	16.1	3.2	80.7	47.3	4.9	4.9	38.1	97.4	2.6	44.7	4.7	50.6	2.1	38.2
	LSFC	17	18.9	8.1	73	64.5	4.8	2.3	32	95.2	4.8	37.0	7.3	55.7	2.5	20.0
	LSFM	16	24.4	2.6	73	70	5.2	9.3	32.6	82.9	17.1	27.9	22.9	49.2	2.6	4.9
	LSM	6	52.3	6.9	40.7	53.7	1.8	7.6	17.5	31.2	68.8	5.2	45.7	49.2	4.7	0.5
	LSMC	15	25	4.5	70.4	57.7	3.9	5.5	36.8	77.8	22.2	25.8	29.5	44.7	2.6	3.5
	LSMF	15	31.5	4.4	64.1	62.1	3.5	7.2	34.5	76.6	23.4	21.1	25.8	53.1	3.2	3.3
Second cycle	LSC	13	11.6	1.1	87.3	59.8	9.4	10.5	28.5	86	14	36.3	23.5	40.2	2.1	6.2
	LSF	17	18.7	0.7	80.5	62	6.4	25.0	44.1	90.4	9.6	32.2	13.8	54.0	2.6	9.4
	LSFC	17	22	3.4	74.6	63.7	5.0	6.6	28.5	95.5	4.5	36.5	6.8	56.8	2.5	21.4
	LSFM	17	23.9	1.1	74.9	64.9	5.2	21.2	38.3	86.9	13.1	31.4	19.0	49.6	2.5	6.6
	LSM	6	45.5	1.3	53.2	63.8	2.7	35.2	18.3	37.4	62.6	6.9	46.4	46.7	4.1	0.6
	LSMC	19	17.8	0.4	81.7	61	6.7	42.1	48.2	96.1	3.9	42.2	6.8	51.0	2.2	24.9
	LSMF	13	39.4	2.9	57.8	49.1	2.3	13.7	32.1	51.1	48.9	11.3	43.3	45.4	3.5	1.0

[a] With respect to C.
[b] Used samples.

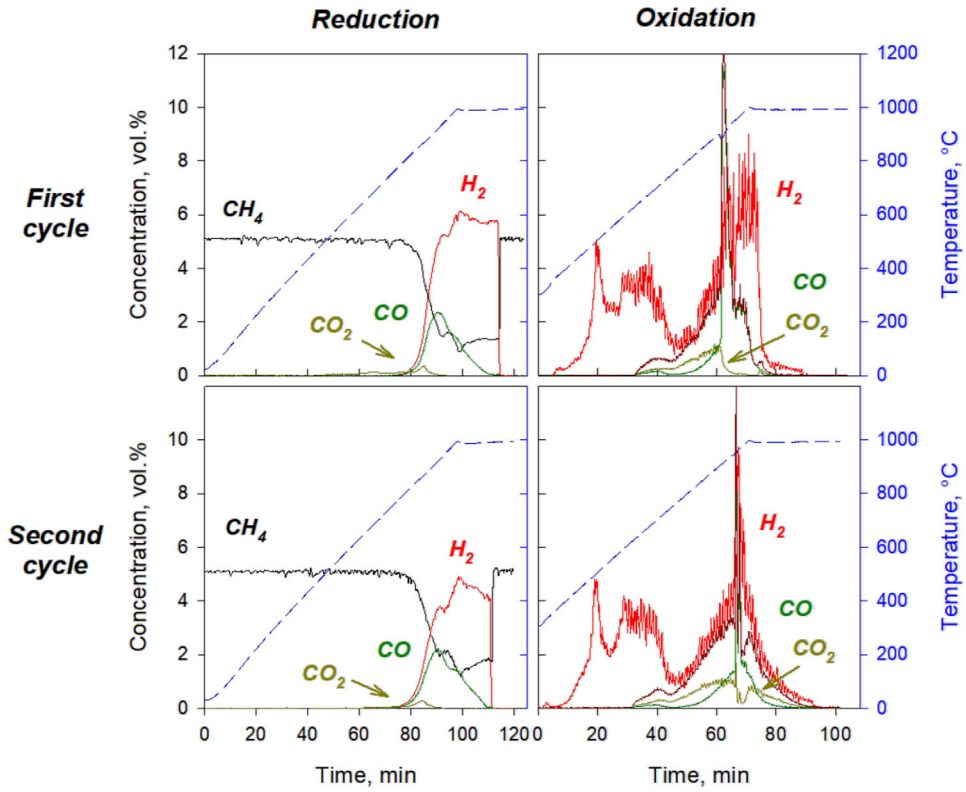

Figure 3. Concentration profiles during TPR/TPO cycles on LSFM.

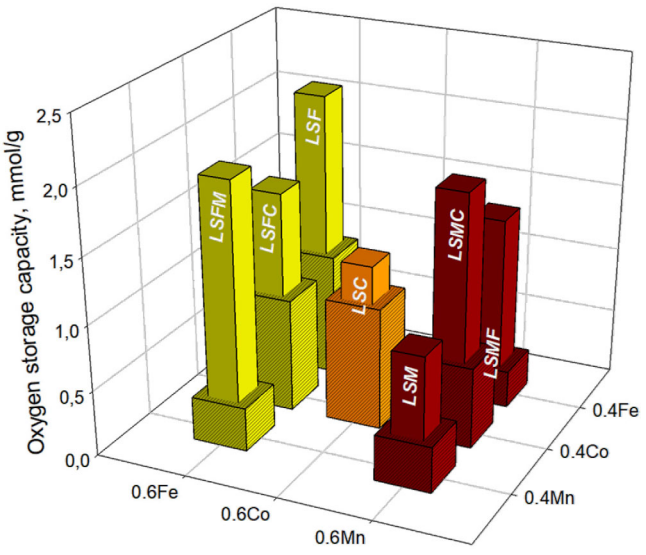

Figure 4. Oxygen storage capacity (OSC) of perovskites in chemical looping reforming of methane (thin bars) and in thermochemical water splitting (thick bars).

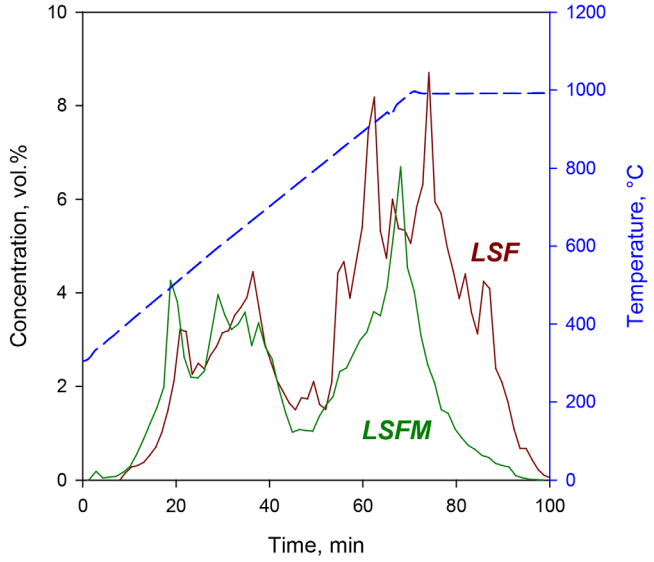

Figure 5. Hydrogen production on LSF and LSFM during TPO (second cycle).

est CH_4 conversion, all the samples show similar activity. The most part of methane is converted into coke; accordingly, the lowest activity of LSM toward methane decomposition partially explains its low conversion. LSC shows different performance between the first and second cycle in terms of exchanged oxygen and products distribution, suggesting a re-organization of the material. The H_2/CO_x ratio during reduction is higher than 2 for the most part of materials; H_2 enrichment with respect to the stoichiometric value of typical CLR is due to the occurrence of methane decomposition, leaving part of carbon as coke onto the material surface.

During oxidation, water conversion is due to both re-oxidation of the material and coke gasification. LSM shows the lowest water conversion, as for methane conversion. CO/CO_2 ratio is generally higher than 1 (except for LSM), due to low selec-

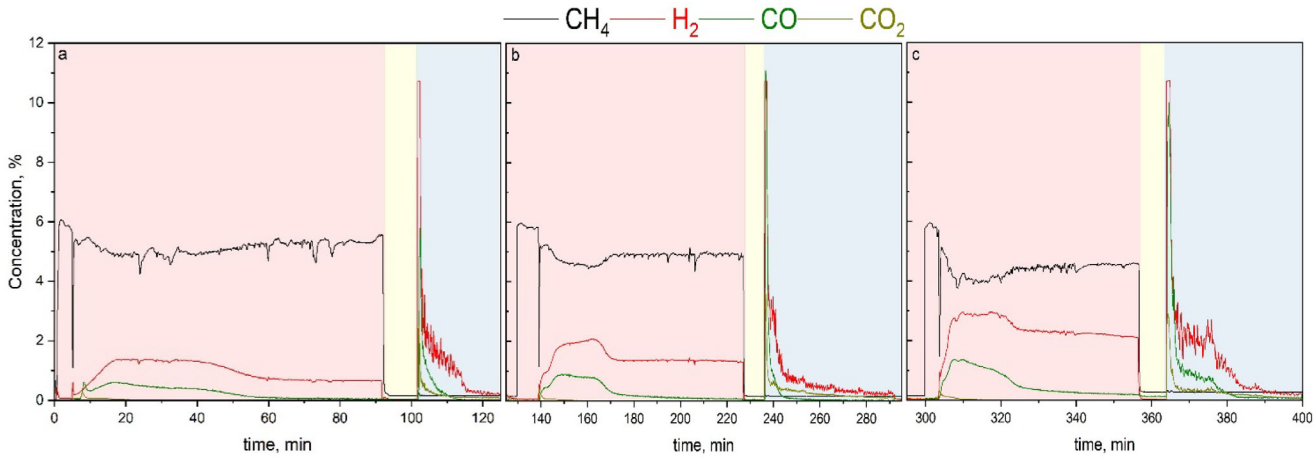

Figure 6. Concentration profiles during isothermal cycles on LSFM for (a) 800, (b) 850, and (c) 900 °C. Reduction, purging, and oxidation are highlighted in red, yellow, and blue areas, respectively.

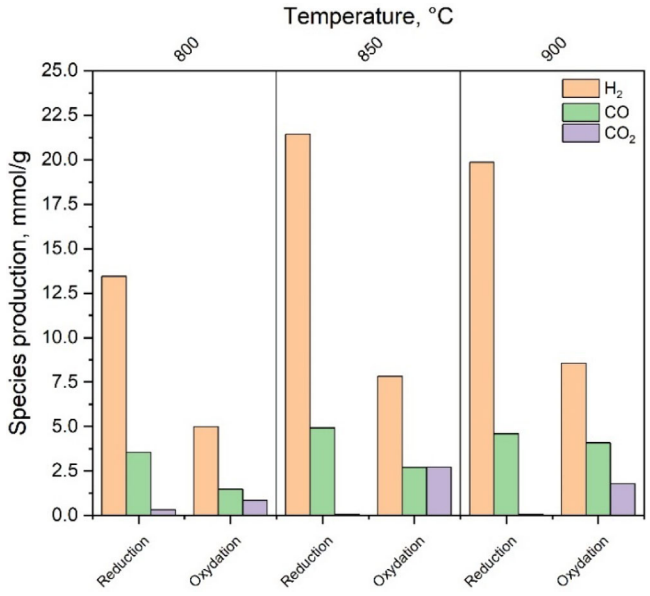

Figure 7. Products distribution per mass of catalyst during isothermal cycles at 800 °C, 850 °C, and 900 °C on LSFM.

tivity to CO_2. The overall H_2/CO_x ratio is higher than 2 (except for LSC). Thus, both steps produce a H_2-rich, CO-rich syngas. Under the adopted operating conditions, H_2O consumption for coke gasification is generally between 40%–60%.

It should be emphasized that the mass balances on carbon and oxygen close within ± 10%. By taking into account the intrinsic error related to the calculation of the produced/consumed amount of reactants/products according to the procedure reported in section CLR tests, the closing of mass balances is satisfying. Finally, O_2-TPO (not reported) carried out on samples after the second TPO revealed the absence of coke still deposited, suggesting that gasification involves all the carbon left during reduction and confirming the overall quality of mass balances.

In their oxidized state, iron and cobalt are 3+,[28] while manganese is 3 + with a 4 + fraction.[37] According to the above results, it appears that CO and CO_2 production start in parallel, suggesting that they are formed onto different metal oxide sites. Cobalt-based perovskites generally possess a larger amount of deep oxidation sites, as suggested by the lower CO/CO_2 ratio (Table 2, second reduction cycle). Partial reduction of metals depletes the deep oxidation of methane to CO_2 and enhances the partial oxidation to CO and H_2. While iron and cobalt can be reduced to their metallic state, manganese is reduced to 2+.[10] Accordingly, LSM shows the lowest OSC (Figure 4). On the other hand, metallic iron and cobalt are more active toward methane decomposition, explaining the larger methane conversion and selectivity to coke of Fe- and Co-containing perovskites. During oxidation, all the materials are re-oxidized at low temperatures, as reported above. Thus, coke oxidation at temperatures above 600 °C is provided by the oxidized metals; during this phase, materials act as catalysts, that is, oxygen provided to coke by the material is fast replaced by water decomposition. LSM shows the lower CO/CO_2 ratio due to its good activity toward full combustion.[37] Among the single metal perovskites, LSF shows the highest selectivity to CO, in agreement with its activity toward partial oxidation.[12] The mixed iron-manganese materials show behavior in between LSF and LSM; the selectivity toward full and partial oxidation seems related to the main metal B cation (i.e., iron or manganese). On the other hand, mixed perovskites containing cobalt are the most selective toward partial oxidation of coke to CO, suggesting a different oxygen availability on these systems compared to material with only a B cation. Further investigation on this behavior is beyond the scope of this work.

Figure 4 shows the OSC of the different materials as calculated according to the second TPR/TPO cycle (thin bars), compared to OSC obtained in simple water splitting (reduction in N_2 up to 1400 °C; thick bars). The use of methane as a reducing agent significantly enhances the OSC of perovskites, independently from the material. LSF and LSFM show the highest OSC.

To decide which material is the most interesting to use in thermal cycles, a comparison between their hydrogen produc-

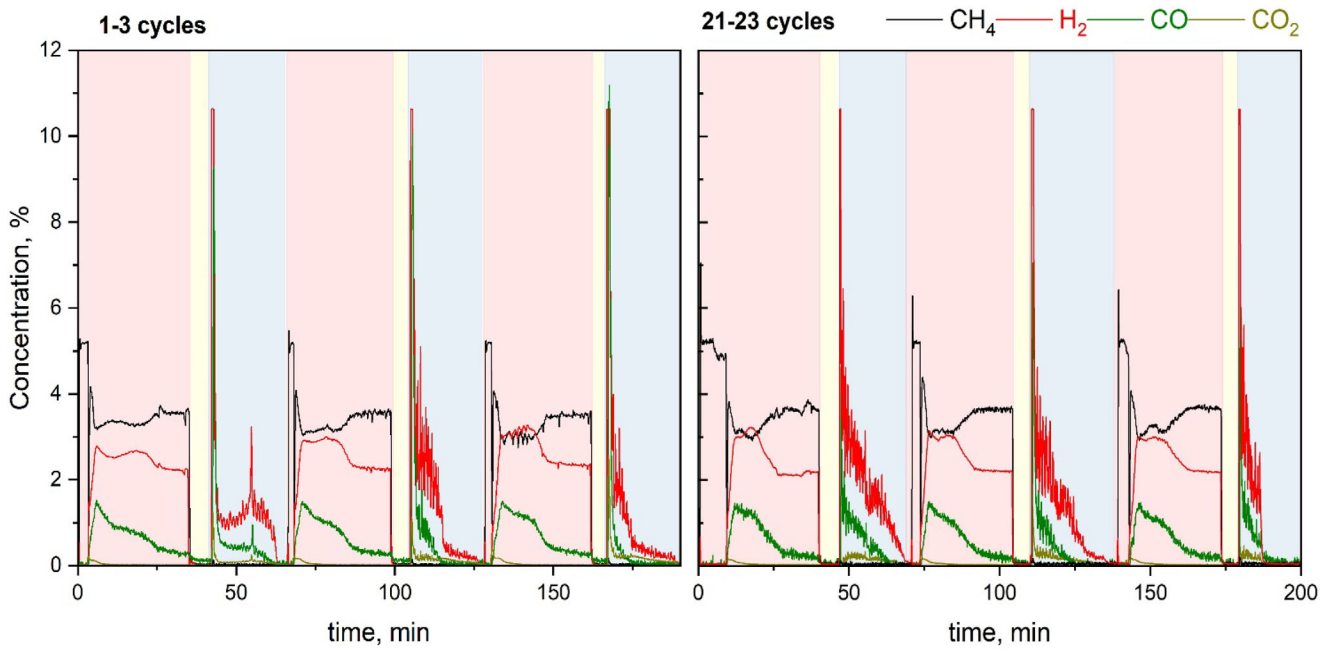

Figure 8. Concentration profiles during first and last isothermal cycles on LSFM at 900 °C. Reduction, purging, and oxidation are highlighted in red, yellow, and blue areas, respectively.

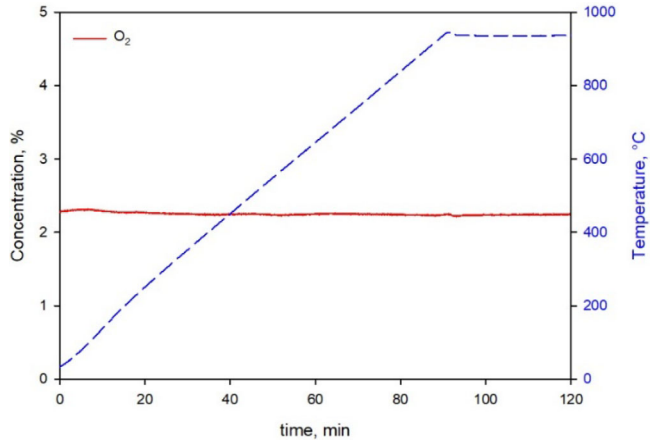

Figure 9. O_2-TPO after 23 isothermal CLR cycles.

tion profiles during TPO has been carried out and reported in Figure 5. Profiles at low temperatures are similar, suggesting similar re-oxidation kinetics. At high temperatures, differences can be noticed; the larger H_2 amount on LSF is due to larger coke deposition and directly related to the large iron content of this sample.[44] However, coke gasification seems faster on LSFM, as suggested by the abrupt decreasing of the corresponding H_2 production. For this reason, LSFM has been selected for further experimentation.

3.2. CLR Cycles

Isothermal cycles are interesting due to their higher energy efficiency.[45–47] To determine the optimal temperature for the isothermal chemical looping cycles, experiments were conducted on the LSFM at three different temperatures: 800 °C, 850 °C, and 900 °C. This temperature range corresponds to the range providing methane conversion during TPR (see section "TPR/TPO") and is typical of CLR.[23,24,48,49]

Figures 6 and 7 show concentration profiles and the products distribution per mass of catalyst during isothermal cycles at different temperatures on LSFM, respectively. Similar reaction trends were observed at all temperatures (Figure 6), although the reaction kinetics and time scales differed. Reduction at 900 °C proceeded rapidly, with an initial peak in CH_4 consumption along with the production of H_2, CO, and CO_2, followed by a noticeable change in the reaction rate, thus giving a slow but steady conversion of methane. The change in the observed reaction rate suggests a change in the reaction mechanism, likely due to the change in the rate-determining step of the process as the catalyst was gradually reduced. The transition to a more gradual and stable methane consumption after the peak can be also attributed to the formation of carbon deposits (as detected during TPR). In contrast to the lower temperatures, the reduction at 900 °C showed a higher consumption of CH_4 and a more pronounced formation of products in a shorter time. During the subsequent oxidation step, a very high increase in the production of H_2, CO, and CO_2 was observed, and peak values for all three gases were reached within 20 min, signaling the complete re-oxidation of the material and gasification of the carbon deposits. Figure 7 shows that the overall quantitative distribution of the reaction products remains almost unchanged between 850 °C and 900 °C, but, as previously described, a notable difference emerges in terms of reaction kinetics. At 900 °C, the reaction time is significantly reduced compared to 850 °C, indicating a more rapid completion of the process.

Based on such observations, 900 °C was selected as the optimum temperature for further chemical looping experiments

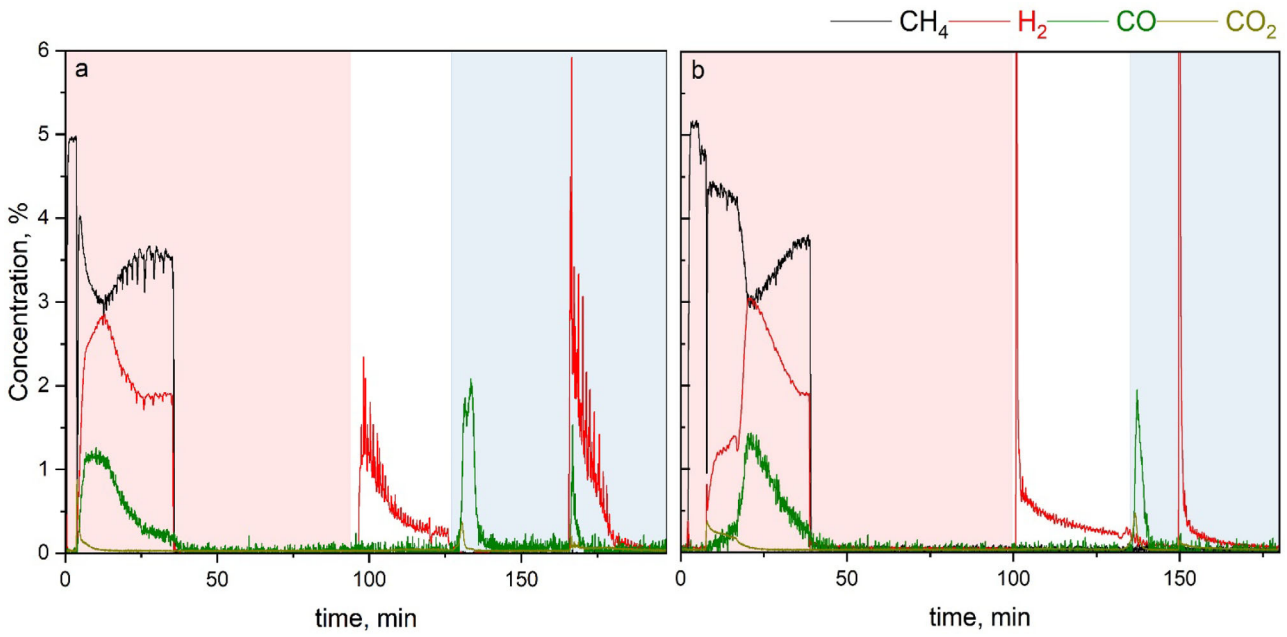

Figure 10. Concentration profiles during (a) first and (b) last non-isothermal three-step cycles on LSFM. Reduction, purging, first oxidation at 550 °C, and second oxidation step are highlighted in red, yellow, and blue areas, respectively.

Table 3. Methane consumption and product production during isothermal two-step cycle and non-isothermal three-step cycle.

Cycle Type	Step	T (°C)	CH_4 Consumption ($mmol/g_{cat}$)	H_2 Production ($mmol/g_{cat}$)	CO Production ($mmol/g_{cat}$)	CO_2 Production ($mmol/g_{cat}$)
Isothermal two-step cycle	Red	900	8.48 ± 0.55	11.4 ± 0.38	3.15 ± 0.21	0.22 ± 0.10
	Ox	900	–	5.25 ± 1.10	1.87 ± 0.30	0.51 ± 0.14
Non-isothermal three-step cycle	Red	900	7.52 ± 1.26	11.37 ± 1.10	3.13 ± 0.07	0.33 ± 0.07
	Ox	550	–	2.67 ± 0.13	–	–
	Ox	900	–	2.65 ± 0.52	1.48 ± 0.36	0.58 ± 0.05

because it would achieve a good conversion of CH_4 and oxidation of carbon within a reduced time frame.

3.3. Isothermal Two-Step Cycles

23 consecutive isothermal reduction-oxidation cycles at an optimized temperature of 900 °C were conducted on the used LSFM material. One cycle consisted of a 30-min reduction phase, followed by a 30-min oxidation phase.

Figure 8 shows the first and last cycles. During each reduction step, the material demonstrated a reproducible production of H_2, CO, and CO_2, along with the generation of carbonaceous deposits (coke). In the following oxidation period, all the coke formed was fully consumed, as proved by the fact that H_2, CO, and CO_2 production ceased.

A very important outcome from the experiments is that LSFM material performed with extraordinary stability over the 23 cycles. As shown in Figure 8, there were no clear signs of deactivation or decay in activity. Thus, the material performed stably, hence showing its durability for long-term use in chemical looping processes under the experimental conditions explored. Additionally, after the 23rd cycle, the O_2-TPO (Figure 9) shows a stable oxygen signal throughout with no uptake of oxygen to indicate residual coke combustion. Moreover, no oxidation of the material is detected, suggesting full re-oxidation under steam.

3.4. Non-Isothermal Three-Step Cycles

It is worth noting that the isothermal cycles provide the production of syngas during both the reduction and oxidation steps. However, the production of pure hydrogen is of interest. The results showed that H_2 production was first noticed at relatively low temperatures (500–600 °C), which was related to the oxidation of the perovskite, while, at high temperatures between 700 and 1000 °C, H_2, CO, and CO_2 were found to be produced simultaneously, resulting from coke gasification. Based on these observations, an innovative three-step cycle is proposed.

1. Reduction in methane at 900 °C (syngas production, material reduction, and carbon deposition).
2. Oxidation in steam at 550 °C (pure hydrogen production and material oxidation).

Table 4. Oxygen storage capacity (OSC) comparison with literature references.

Materials	OSC (mmol/g)	References
$LaMn_{0.7}Fe_{0.3}O_3$	3.0	[36]
$LaFeO_3$-CeO_2	2.7	[21]
3DOM $LaFeO_3$	1.6	[48]
$LaSrFeCoO_6$	5.9	[27]
$La_{0.6}Sr_{0.4}Mn_{0.5}Co_{0.5}O_{3+\delta}$	3.2[a)]	[38]
$LaMn_{1-x}Al_xO_{3+\delta}$	2.0	[37]
$La_{0.6}Sr_{0.4}Fe_{0.6}Mn_{0.4}O_3$	2.3	This work

[a)] Measured by H_2-TPR.

3. Oxidation in steam at 900 °C (syngas production and coke gasification).

The catalyst went through eight such cycles (Figure 10 shows the first and last ones), and the expected results were confirmed. The reduction step at 900 °C exhibited behavior consistent with the isothermal process, with CH_4 consumption leading to the formation of H_2, CO, and CO_2, alongside carbonaceous deposits on the material. At 550 °C, only hydrogen evolved due to the oxidation of the perovskite, while at 900 °C, coke gasification took place during the reduction reaction, with H_2, CO, and CO_2 evolving simultaneously. More importantly, the material remained stable, and no serious deactivation was observed after eight cycles of operation.

At the end of the 8th cycle, an O_2-TPO (not reported) was performed, as previously described, confirming the absence of coke and full oxidation of the sample at the end of the CLR cycles.

Table 3 shows the average methane consumption and product production per gram of catalyst per cycle during the whole experimental campaign.

A straightforward comparison with literature results is quite difficult due to the variability of experimental conditions and of performance parameters. For instance, methane conversion strictly depends on contact time and thus, values obtained at different contact times cannot be compared. On the other hand, the OSC could be considered more representative of the material's performance. Table 4 shows some OSC calculated from literature results. LSFM shows OSC similar to those reported in the literature; only the double Fe-Co perovskite[36] shows a significantly higher oxygen evolution. Interestingly, the overall H_2 and CO productivity is about 16.7 and 5.0 mmol/g, independent of the type of cycle (2 or 3 steps). The H_2/CO ratio is about 3, in agreement with the stoichiometry of reforming reaction. In comparing the LSFM performance against novel metal oxide-based systems, such as Ni-modified WO_3 systems,[16] it is important to consider the different operating conditions applied. While Ni-WO_3/ZrO_2 catalysts have shown considerable activity under milder conditions, the LSFM perovskite evaluated in this work exhibited comparable or even superior syngas production under more severe conditions. This indicates that, while Ni-WO_3-based is highly effective in their optimized conditions, perovskite-like catalyst can also be a worthy candidate for CLR. Notably, the LSFM showed constant performance during 45 h of time-on-stream, with no deactivation signs, and even showed a progressive structural homogenization of the perovskite phase.

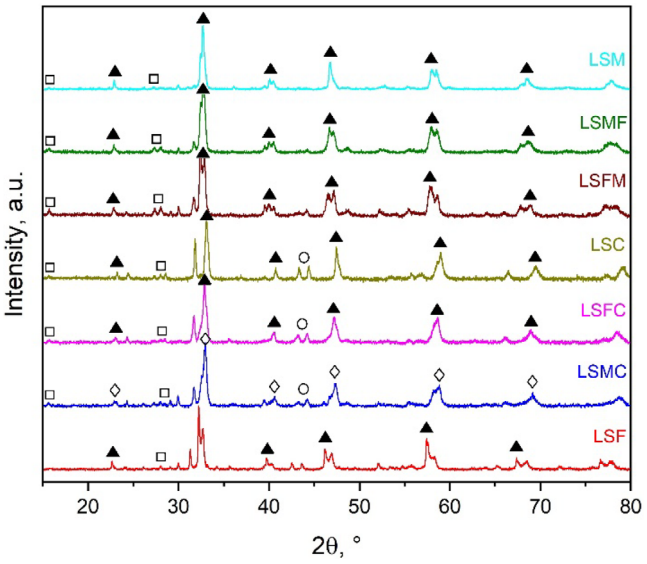

Figure 11. XRD profiles of studied perovskites: (▲) trigonal R-3c perovskite-like phase, (◊) cubic Pm-3 m perovskite-like phase, (□) lanthanum oxide phase (JCPDS 01–071–5408), and (°) lanthanum-cobalt oxide (JCPDS 00–034–1081).

Furthermore, application of perovskite-type materials is highly compatible with the innovative three-step two-temperature approach proposed in this study, thanks to their ability to store oxygen at relatively low temperatures (below 550 °C).

3.5. Characterization of the Materials

Figure 11 shows XRD profiles of the studied perovskites, revealing a complex phase composition influenced by the nature of the B-site cation. In all samples, reflections associated with La_2O_3 (JCPDS 01–071–5408 and JCPDS 00–054–0213) were detected in the range $2\theta = 15°–30°$, indicating the presence of a segregated lanthanum oxide phase due to the low calcination temperature (~1100 °C). Additionally, a distinctive peak at approximately $\theta = 45°$ appears in the cobalt-containing perovskites, suggesting the formation of an orthorhombic lanthanum-cobalt oxide (JCPDS 00–034–1081) as a secondary phase.

Apart from the secondary oxide phases, the dominant reflections in the XRD patterns are those of perovskite-like structures, which differ according to the specific transition metal used as the B-site. LSC, LSF, LSM, LSFC, and LSMF consist mainly of a trigonal R-3c phase (JCPDS 00–048–0122, JCPDS 01–090–0939, JCPDS 01–09–8874, JCPDS 01–090–8920, JCPDS 04–015–50219, respectively). The presence of two phases, both with a trigonal R-3c:H structure (JCPDS 00–072–0089 and JCPDS 00–074–0744), was verified in LSFM; LSMC, however, breaks the trend and is cubic with a Pm-3m structure (JCPDS 00–069–0224).

The results emphasize the impact of the B-site cations and reveal that, although most of the perovskites investigated here follow the rhombohedral R-3c:H symmetry, the introduction of

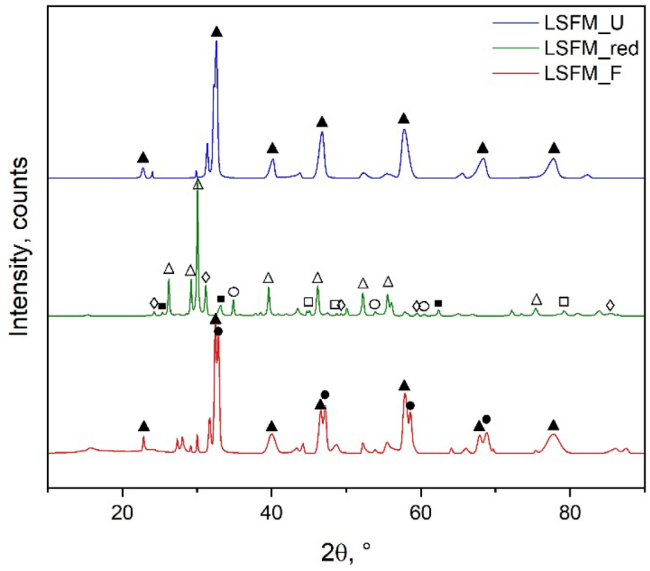

Figure 12. XRD profiles of fresh, used and reduced LSFM (LSFM_F, LSFM_U, LSFM_red, respectively): (▲) trigonal R-3c perovskite-like phase (JCPDS 00–072–0089), (●) trigonal R-3c perovskite-like phase (JCPDS 00–074–0744), (Δ) trigonal P-3m1 La_2O_3 phase (JCPDS 04–008–7342), (◊) tetragonal I41/amd Mn_3O_4 phase (JCPDS 03–065–2776), (□) orthorhombic Pbcm Fe (JCPDS 04–018–8483), (°) cubic Fm-3m SrO (JCPDS 01–071–3778), and (■) trigonal R-3c Fe(CO_3) (JCPDS 04–018–4705).

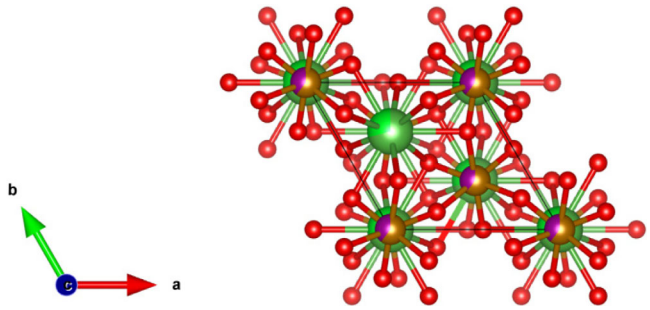

Figure 13. Crystal structure of the predominant phase in LSFM perovskite (JCPDS 00–072–0089). The image was obtained using VESTA software.

certain transition metals, like cobalt, facilitates the development of other phases with unique crystallographic features.[12] The presence of the R-3c:H space group is consistent with theoretical expectations using the Goldschmidt tolerance factor (as in the preceding section), further corroborating the structural stability of these perovskites.

The XRD analysis of LSFM in its fresh, used (after 30 cycles), and reduced forms (Figure 12) reveals significant phase evolution while retaining a consistent rhombohedral symmetry (R-3c:H). Fresh LSFM catalyst is predominantly composed of the LSFMO phase (JCPDS 00–072–0089) (crystal structure in Figure 13), with minor contributions of other perovskite-like phases (iron-free) and La_2O_3. After 30 redox cycles, the overall perovskite structure remains intact, as shown by the retention of the main diffraction peaks (JCPDS 00–072–0089). Significant phase transformation occurs, most notably the loss of La_2O_3 reflections, indicating the complete incorporation of lanthanum into the perovskite lattice. Additionally, peaks that were originally related to minor perovskite-like iron-free phases also decreased, indicating a gradual restructuring and uniformization and preferring iron-enriched perovskite phases.

Conversely, the reduced LSFM sample, which experienced a reduction step in CH_4 without subsequent reoxidation, exhibits some differences in the XRD spectra. The perovskite lattice characteristic reflections are weakened, and other peaks corresponding to metallic Fe phases, La, Mn, Sr oxides, and Fe-carbonate are observed, revealing the partial decomposition of the perovskite structure under reducing conditions. Furthermore, intermediate oxide phases not related to the perovskite lattice emerged. XRD analysis does not reveal the presence of carbon phases on the material, despite the expected coke deposition after the reduction step; this suggests that the carbon produced is likely to be in its amorphous phase, undetectable by XRD.

The presence of iron carbonate ($FeCO_3$) can be attributed to CO_2 adsorption onto the material during the reduction step, where it remains stabilized in this carbonate form. In the oxidation phase, Fe^{2+} in $FeCO_3$ is oxidized to Fe^{3+}, releasing CO_2,[50] which can further contribute to gasification reactions, promoting CO formation through the Boudouard reaction. According to El-Bellihi,[50] iron carbonate decomposition occurs at about 600 °C, thus during the second oxidation step of the three-step cycle; this is experimentally confirmed by the absence of CO_x during the first oxidation step (see section "Non-isothermal three-step cycles"). It is reasonable to suppose that the amount of iron carbonate is limited and confined to the outer shell of LSFM material, thus releasing low amounts of carbon dioxide and providing an additional minor contributor to the overall material oxidation. Interestingly, no carbon phase is detected on the reduced sample, suggesting the formation of amorphous carbon.

These results show that while LSFM retains its perovskite structure with repeated redox cycles, reduction alone results in extreme structural decomposition. The stability of the rhombohedral phase in fresh and used samples indicates its robustness under cycling conditions, whereas the breakdown of the perovskite network in reduced LSFM highlights the deep modification of the material under reducing conditions; however, oxidation in steam fully restores the perovskite structure, thus suggesting a complete reversibility between the reduced and oxidized LSFM.

4. Conclusions

Perovskites with the general formula $La_{0.6}Sr_{0.4}B_xB'_{1-x}O_3$ (*B*, B′ = Fe, Co, Mn) were prepared and tested for chemical looping reforming (CLR) of methane. Preliminary tests conducted through temperature-programmed reduction (TPR) in methane and temperature-programmed oxidation (TPO) in steam revealed that the redox properties of perovskite can be tuned by the proper combination of different B cations. Materials with different B cations showed higher oxygen storage capacity (OSC) with respect to their single B cation counterparts, showing that this strategy allows to improve the oxygen amount that can

be released. Interestingly, CLR reaction conditions, that is, the use of (bio)methane as a reductant up to 1000 °C, enlarges OSC with respect to self-reduction at 1300 °C; moreover, the operating temperature of the reduction step is significantly lower.

During the reduction step, most of the materials showed good selectivity toward partial oxidation products (i.e., syngas) rather than CO_2 and H_2O; moreover, at a high reduction degree of the perovskites, methane is decomposed to additional hydrogen and coke. TPO revealed that full oxidation of the perovskites occurs at low temperatures (<600 °C), while coke gasification occurs at higher temperatures. At the end of TPR/TPO cycles, the perovskites are fully oxidized and coke-free.

The most interesting material ($La_{0.6}Sr_{0.4}Fe_{0.6}Mn_{0.4}O_3$, LSFM) was tested in repeated isothermal cycles at 900 °C, selected as the best operating temperature. Performance in terms of product amounts distribution and production rates is stable, suggesting the full stability of this perovskite.

Moreover, the results of TPR/TPO experiments suggested an innovative 3-step cycle composed by a reduction in methane at 900 °C (syngas production, material reduction, carbon deposition), an oxidation in steam at 550 °C (pure hydrogen production, material oxidation), and an oxidation in steam at 900 °C (syngas production, coke gasification). LSFM was successfully tested in this novel cycle, showing pure hydrogen production during the second step and syngas production during steps 1 and 3. Performance was stable in repeated experiments.

Characterizations revealed that materials show that the main structure corresponds to perovskite phase. However, the low calcination temperature does not provide full formation of a single perovskite structure. The repeated use of LSFM showed a reorganization of the material with improved perovskites structure; this phenomenon does not modify the overall performance, suggesting that usage conducts to a more stable phase structure with the same OSC. Under reducing reaction conditions, iron and manganese are reduced. Metallic iron is detected; the presence of a single perovskite phase after oxidation suggests the full reversibility of the phase transition between reduced and oxidized LSFM material.

Acknowledgements

The Research Agreement (POR)-PNRR–"Hydrogen Research–Mission M2-C2–Investment 3.5: Research and Development on Hydrogen, WP1–LA1.1.34: Development of non-critical materials and components for tandem photoelectrolysis cells for direct conversion of solar energy into hydrogen and advanced systems for solar- and thermal-assisted catalytic splitting", funded by the Italian Ministry of Ecological Transition (MITE) is particularly acknowledged for funding this work. A. Basco and S. Scognamiglio thank the project funded by the European Union–NextGenerationEU under the National Recovery and Resilience Plan (NRRP), Mission 4 "Education and Research"–Component 2 "From research to business"–Investment 3.1 "Fund for the realization of an integrated system of research and innovation infrastructures" – Call n. 3264 of December 28, 2021, of Italian Ministry of University and Research | Award Decree n. 128 (June 21, 2022)–Project code: IR0000027–CUP: B33C22000710006–Project title: iENTRANCE@ENL: Infrastructure for Energy Transition and Circular Economy @ EuroNanoLab. The authors gratefully acknowledge Mr. Andrea Capuozzo and Mr. Luigi Stanzione for XRF, N_2 physisorption, and XRD measurements.

Open access publishing facilitated by Consiglio Nazionale delle Ricerche, as part of the Wiley - CRUI-CARE agreement.

Conflict of Interests

The authors declare no conflict of interest.

Data Availability Statement

The data that support the findings of this study are available from the corresponding author upon reasonable request.

Keywords: Biomethane · Chemical looping reforming · Environmental chemistry · Hydrogen · Oxygen carrier

[1] R. Kumar, R. Singh, S. Dutta, *Energy Fuels* **2024**, *38*, 2601–2629.
[2] B. S. Zainal, P. J. Ker, H. Mohamed, H. C. Ong, I. M. R. Fattah, S. M. A. Rahman, L. D. Nghiem, T. M. I. Mahlia, *Renew. Sustain. Energy Rev.* **2024**, *189*, 113941.
[3] A. Alamiery, *ChemPhysMater* **2024**, *3*, 64–73.
[4] S. Zhironkin, M. Cehlár, *Energies (Basel)* **2023**, *16*, 4193.
[5] Y. De Vos, M. Jacobs, P. Van Der Voort, I. Van Driessche, F. Snijkers, A. Verberckmoes, *Catalysts* **2020**, *10*, 926.
[6] L. André, S. Abanades, G. Flamant, *Renew. Sustain. Energy Rev.* **2016**, *64*, 703–715.
[7] C. Agrafiotis, M. Roeb, C. Sattler, *Renew. Sustain. Energy Rev.* **2015**, *42*, 254–285.
[8] D. Yadav, R. Banerjee, *Renew. Sustain. Energy Rev.* **2016**, *54*, 497–532.
[9] J. E. Lee, I. Shafiq, M. Hussain, S. S. Lam, G. H. Rhee, Y. K. Park, *Int. J. Hydrogen Energy* **2022**, *47*, 4346–4356.
[10] M. Orfila, M. Linares, R. Molina, J. Á. Botas, R. Sanz, J. Marugán, *Int. J. Hydrogen Energy* **2016**, *41*, 19329–19338.
[11] R. R. Bhosale, G. Takalkar, P. Sutar, A. Kumar, F. AlMomani, M. Khraisheh, *Int. J. Hydrogen Energy* **2019**, *44*, 34–60.
[12] T. Dawa, B. Sajjadi, *Fuel Process. Technol.* **2024**, *253*, 108022.
[13] H. X. Zhang, Z. Q. Huang, B. Yang, C. R. Chang, *Chem. Eng. Sci.* **2022**, *262*, 118041.
[14] J. Guerrero-Caballero, T. Kane, L. Jalowiecki-Duhamel, A. Löfberg, *Catal. Today* **2019**, *333*, 251–258.
[15] M. Tang, L. Xu, M. Fan, *Appl. Energy* **2015**, *151*, 143–156.
[16] S. Miyazaki, Z. Li, T. Toyao, Y. Nakasaka, Y. Nakajima, K. Shimizu, Z. Maeno, *Energy and Fuels* **2023**, *37*, 7945–7957.
[17] J. López van der Horst, M. Volpe Giangiordano, F. Suarez, F. Perez, M. Gatti, G. Santori, F. Pompeo, *Reactions* **2025**, *6*, 5.
[18] R. R. Bhosale, A. Kumar, A. Ashok, P. Sutar, G. Takalkar, M. Khraisheh, F. Almomani, U. Ghosh, *MRS Adv.* **2017**, 3365–3370.
[19] M. M. Nair, S. Abanades, *Sustain. Energy Fuels* **2018**, *2*, 843–854, https://doi.org/10.1039/C7SE00516D.
[20] A. Bayon, A. de la Calle, K. K. Ghose, A. Page, R. McNaughton, *Int. J. Hydrogen Energy* **2020**, *45*, 12653–12679.
[21] D. Cao, C. Luo, F. Wu, L. Zhang, X. Li, *J. Environ. Chem. Eng.* **2022**, *10*, 107315.
[22] F. He, K. Zhao, Z. Huang, X. Li, G. Wei, H. Li, *Chin. J. Catal.* **2013**, *34*, 1242–1249.
[23] Y. Shen, K. Zhao, F. He, H. B. Li, *J. Fuel Chem. Technol.* **2016**, *44*, 1168–1176.

[24] D. Sastre, D. P. Serrano, P. Pizarro, J. M. Coronado, *J. CO2 Util.* **2019**, *31*, 16–26.
[25] F. He, J. Chen, S. Liu, Z. Huang, G. Wei, G. Wang, Y. Cao, K. Zhao, *Int. J. Hydrogen Energy* **2019**, *44*, 10265–10276.
[26] F. He, X. Li, K. Zhao, Z. Huang, G. Wei, H. Li, *Fuel* **2013**, *108*, 465–473.
[27] K. Zhao, Y. Shen, Z. Huang, F. He, G. Wei, A. Zheng, H. Li, Z. Zhao, *J. Energy Chem.* **2017**, *26*, 501–509.
[28] K. Zhao, J. Chen, H. Li, A. Zheng, F. He, *J. Energy Inst.* **2019**, *92*, 594–603.
[29] K. Zhao, A. Zheng, H. Li, F. He, Z. Huang, G. Wei, Y. Shen, Z. Zhao, *Appl. Catal. B* **2017**, *219*, 672–682.
[30] K. ZHAO, Y. SHEN, F. HE, Z. HUANG, G. WEI, A. ZHENG, H. LI, Z. ZHAO, *J. Rare Earths* **2016**, *34*, 1032–1041.
[31] K. Zhao, L. Li, A. Zheng, Z. Huang, F. He, Y. Shen, G. Wei, H. Li, Z. Zhao, *Appl. Energy* **2017**, *197*, 393–404.
[32] K. Zhao, F. He, Z. Huang, G. Wei, A. Zheng, H. Li, Z. Zhao, *Appl. Energy* **2016**, *168*, 193–203.
[33] K. Zhao, R. Zhang, Y. Gao, Y. Lin, A. Liu, X. Wang, A. Zheng, Z. Huang, Z. Zhao, *Fuel Process. Technol.* **2022**, *236*, 107398.
[34] Z. Yang, Y. Zheng, K. Li, Y. Wang, Y. Wang, H. Wang, Y. Wang, L. Jiang, X. Zhu, Y. Wei, *Chem. Eng. Sci.* **2021**, *229*, 116085.
[35] Y. Zheng, L. Zhao, Y. Wang, Y. Wang, H. Wang, Y. Wang, L. Jiang, X. Zhu, Y. Wei, K. Li, *Fuel Process. Technol.* **2021**, *215*, 106744.
[36] X. Yin, S. Wang, B. Wang, L. Shen, *Chem. Eng. J.* **2021**, *422*, 128751.
[37] X. Yin, S. Wang, B. Wang, L. Shen, *Int. J. Hydrogen Energy* **2021**, *46*, 33375–33387.
[38] X. Yin, L. Shen, S. Wang, B. Wang, C. Shen, *Appl. Catal. B* **2022**, *301*, 120816.
[39] G. Luciani, G. Landi, A. Aronne, A. Di Benedetto, *Sol. Energy* **2018**, *171*, 1–7.
[40] Z. Li, M. Yang, J. S. Park, S. H. Wei, J. J. Berry, K. Zhu, *Chem. Mater.* **2016**, *28*, 284–292.
[41] P. S. Barbato, V. Di Sarli, G. Landi, A. Di Benedetto, *Chem. Eng. J.* **2015**, *259*, 381–390.
[42] G. Saracco, F. Geobaldo, G. Baldi, *Appl. Catal. B* **1999**, *20*, 277–288.
[43] S. Li, R. Kato, Q. Wang, T. Yamanaka, T. Takeguchi, W. Ueda, *Appl. Catal. B* **2010**, *93*, 383–386.
[44] J. Yang, E. Bjørgum, H. Chang, K. K. Zhu, Z. J. Sui, X. G. Zhou, A. Holmen, Y. A. Zhu, D. Chen, *Appl. Catal. B* **2022**, *301*, 120788.
[45] L. Zhu, Y. Lu, *Energy and Fuels* **2018**, *32*, 736–746.
[46] I. Al-Shankiti, B. D. Ehrhart, A. W. Weimer, *Sol. Energy* **2017**, *156*, 21–29.
[47] Y. Hao, C.-K. Yang, S. M. Haile, *Phys. Chem. Chem. Phys.* **2013**, *15*, 17084.
[48] K. Zhao, F. He, Z. Huang, A. Zheng, H. Li, Z. Zhao, *Int. J. Hydrogen Energy* **2014**, *39*, 3243–3252.
[49] K. Zhao, F. He, Z. Huang, G. Q. Wei, A. Q. Zheng, H. Bin Li, Z. L. Zhao, *J Fuel Chem Technol.* **2016**, *44*, 680–688.
[50] A. El-Bellihi, *J. Chem.* **2010**, *53*, 871–884.

Manuscript received: March 27, 2025
Revised manuscript received: May 23, 2025
Accepted manuscript online: May 24, 2025
Version of record online: June 16, 2025